This is the peer-reviewed, final accepted version for American Mineralogist, published by the Mineralogical Society of America.
The published version is subject to change. Cite as Authors (Year) Title. American Mineralogist, in press.
DOI: https://doi.org/10.2138/am-2024-9410. http://www.minsocam.org/

Revision 1

Phase transformation of ferric-iron-rich silicate in Earth's mid-mantle

Mingda Lv[1], Shengcai Zhu[2*], Jiachao Liu[1], Yi Hu[3,4], Feng Zhu[5,6], Xiaojing Lai[3,4,7], Dongzhou Zhang[3], Bin Chen[3], Przemyslaw Dera[3], Jie Li[5], and Susannah M. Dorfman[1*]

[1] Department of Earth and Environmental Sciences, Michigan State University, East Lansing, MI, USA

[2] School of Materials, Sun Yat-Sen University, Guangzhou, China

[3] Hawai'i Institute of Geophysics and Planetology, University of Hawai'i at Mānoa, Honolulu, HI, USA

[4] Department of Geology and Geophysics, School of Ocean and Earth Science and Technology, University of Hawai'i at Mānoa, Honolulu, HI, USA

[5] Department of Earth and Environmental Sciences, University of Michigan, Ann Arbor, MI, USA

[6] State Key Laboratory of Geological Processes and Mineral Resources, School of Earth Sciences, China University of Geosciences, Wuhan, Hubei, China

[7] Gemological Institute, China University of Geosciences, Wuhan, Hubei, China

[*] Corresponding authors: S.M. Dorfman (dorfman3@msu.edu) and S. Zhu (zhushc@mail.sysu.edu.cn)

This is the peer-reviewed, final accepted version for American Mineralogist, published by the Mineralogical Society of America.
The published version is subject to change. Cite as Authors (Year) Title. American Mineralogist, in press.
DOI: https://doi.org/10.2138/am-2024-9410. http://www.minsocam.org/

Abstract

Incorporation of ferric iron in mantle silicates stabilizes different crystal structures and changes phase transition conditions, thus impacting seismic wave speeds and discontinuities. In $MgSiO_3$-Fe_2O_3 mixtures, recent experiments indicate the coexistence of fully oxidized iron-rich $(Mg_{0.5}Fe_{0.5}^{3+})(Fe_{0.5}^{3+}Si_{0.5})O_3$ with Fe-poor silicate (wadsleyite or bridgmanite) and stishovite at 15 to 27 GPa and 1773 to 2000 K, conditions relevant to subducted lithosphere in the Earth's transition zone and uppermost lower mantle. X-ray diffraction measurements show that $(Mg_{0.5}Fe_{0.5}^{3+})(Fe_{0.5}^{3+}Si_{0.5})O_3$ recovered from these conditions adopts the R3c $LiNbO_3$-type structure, which transforms to the bridgmanite structure again between 18.3 GPa and 24.7 GPa at 300 K. Diffraction observations are used to obtain the equation of state of the $LiNbO_3$-type phase up to 18.3 GPa. These observations combined with multi-anvil experiments suggest that the stable phase of $(Mg_{0.5}Fe_{0.5}^{3+})(Fe_{0.5}^{3+}Si_{0.5})O_3$ is bridgmanite at 15-27 GPa, which transforms on decompression to $LiNbO_3$-type structure. Our calculation revealed that ordering of the ferric ion reduces the kinetic energy barrier of the transition between $(Mg_{0.5}Fe_{0.5}^{3+})(Fe_{0.5}^{3+}Si_{0.5})O_3$ $LiNbO_3$ structure and bridgmanite relative to the $MgSiO_3$ akimotoite-bridgmanite system. Dense Fe^{3+}-rich bridgmanite structure is thus stable at substantially shallower depths than $MgSiO_3$ bridgmanite and would promote subduction.

1 Introduction

Mineralogical differences due to chemical heterogeneity in the mantle are crucial for understanding the dynamics of mantle convection and driving forces for plate tectonics (Stixrude and Lithgow-Bertelloni 2012; Faccenda and Dal Zilio 2017). The average oxygen fugacity of the upper mantle has been underestimated (Cottrell and Kelley 2011), and orders of magnitude heterogeneity in mantle oxygen fugacity suggest that both subduction and plumes oxidize the mantle (Cottrell and Kelley 2013; Moussallam et al. 2019; Cottrell et al. 2021). Local iron enrichment and high oxygen fugacity may be also found in regions containing subducted basalt and hematite-rich sediment. These variations in oxidation of the mantle may impact the stability and equilibrium composition of major mantle minerals (e.g. Gu et al. 2016), with corresponding effects on seismic velocities and dynamics of downwelling slabs and upwelling plumes.

Recent experiments (Wang et al. 2021; Chanyshev et al. 2023) indicate that under oxidizing conditions in the transition zone and uppermost lower mantle, Fe^{3+} may partition out of

dominant silicates wadsleyite, ringwoodite, and bridgmanite into a separate dense phase. In bulk compositions with 90-93% $MgSiO_3$ and 7-10% Fe_2O_3, experiments at 15-27 GPa and 1773-2000 K produce $(Mg_{0.5}Fe_{0.5}^{3+})(Fe_{0.5}^{3+}Si_{0.5})O_3$ coexisting with wadsleyite and stishovite or bridgmanite and stishovite. Because the Fe^{3+}-rich phase forms within a much less Fe-rich bulk composition, it could be found in oxidized natural lithologies. However, these studies did not observe the structure of $(Mg_{0.5}Fe_{0.5}^{3+})(Fe_{0.5}^{3+}Si_{0.5})O_3$ in situ at high pressure and temperature. Identifying this phase, its stability range, and physical properties is important to determining the mineralogy of oxidized mantle and its impact on geophysics.

$(Mg_{0.5}Fe_{0.5}^{3+})(Fe_{0.5}^{3+}Si_{0.5})O_3$ recovered from lower mantle pressures exhibits a structure within the corundum family, a group of minerals with related structures and multiple possible cation orderings including corundum Al_2O_3 and hematite Fe_2O_3 (space group $R\bar{3}c$), hemleyite $FeSiO_3$ and ilmenite $FeTiO_3$ (space group $R\bar{3}$), $LiNbO_3$-type wangdaoite $FeTiO_3$ (space group $R3c$) (Navrotsky 1998; Dubrovinsky et al. 2009; Bindi et al. 2017; Xie et al. 2020), and an $R3$ modified corundum structure similar to the $LiNbO_3$-type structure (Koemets et al. 2023) (**Figure 1**). Both $LiNbO_3$-type and ilmenite-type structures have two octahedral cation sites with different sizes, denoted as AO_6 (A site) and BO_6 (B site), respectively. Cation ordering as in $LiNbO_3$ makes this structure approach a distorted perovskite, and thus promotes its transition to bridgmanite (orthorhombic perovskite) with a very low energy barrier (Navrotsky 1998). The synthesis and phase transition of $LiNbO_3$-type $(Mg_{0.5}, Fe_{0.5}^{3+})(Si_{0.5}, Al_{0.5}^{3+})O_3$ has also been reported (Liu et al. 2019; Zhu et al. 2020; Koemets et al. 2023). Fe^{3+} can simultaneously substitute for Mg^{2+} and Si^{4+} in compositions along the $MgSiO_3$–Fe_2O_3 join. In contemporary experiments to this work, $(Mg_{0.5}Fe_{0.5}^{3+})(Fe_{0.5}^{3+}Si_{0.5})O_3$ was identified with the $R3c$ $LiNbO_3$-type structure (Chanyshev et al. 2023), but additional single-crystal diffraction suggests reassigning this material to the $R3$ structure (Koemets et al. 2023). Analysis of natural akimotoite and hemleyite in chondritic meteorites (Sharp et al. 1997; Tomioka and Fujino 1997) demonstrates incorporation of Fe and Al in the ilmenite-structured silicate up to at least 50% Fe^{2+} in substitution for Mg^{2+} on the A site, above the solubility limit determined by experiment (Ito and Yamada 1982). Pressure can drive cation reordering transitions between the ilmenite and $LiNbO_3$-type structures (Ko and Prewitt 1988), and the closely-related structures may be difficult to distinguish with diffraction.

This is the peer-reviewed, final accepted version for American Mineralogist, published by the Mineralogical Society of America.
The published version is subject to change. Cite as Authors (Year) Title. American Mineralogist, in press.
DOI: https://doi.org/10.2138/am-2024-9410. http://www.minsocam.org/

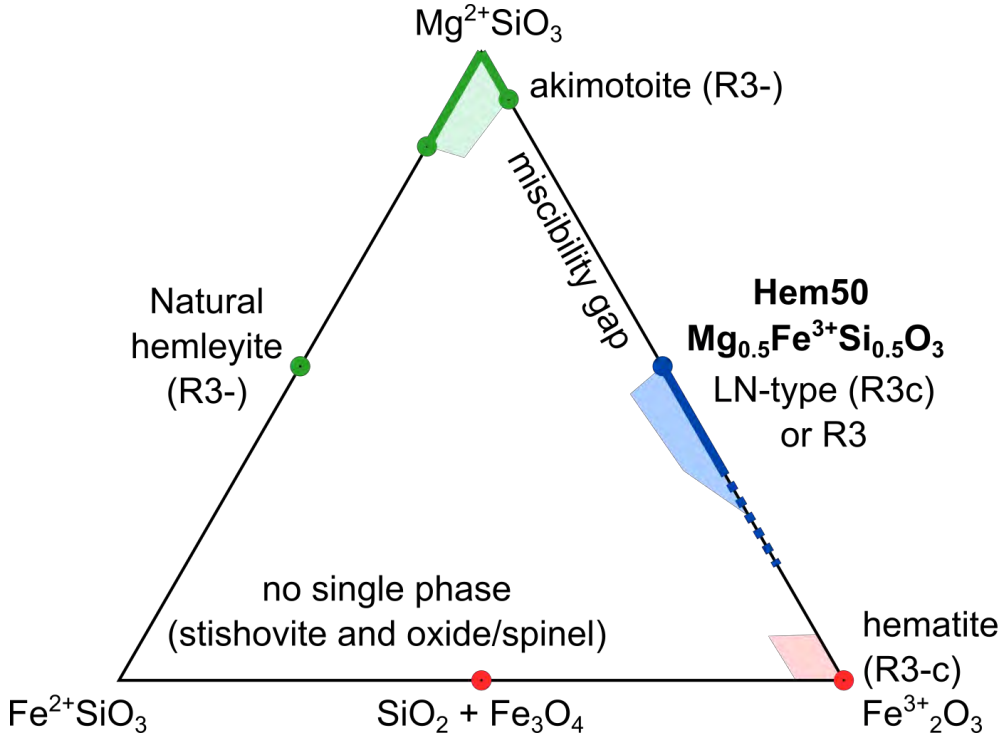

Figure 1. Schematic diagram summarizing known compositions and structures of compounds in the $MgSiO_3$-$Fe^{2+}SiO_3$-$Fe^{3+}{}_2O_3$ system at ~20-24 GPa. For $MgSiO_3$ and Fe_2O_3 end-members, stable structures at subducted slab conditions are $R\bar{3}$ akimotoite and $R\bar{3}c$ hematite, respectively. For compositions at or near the $FeSiO_3$ end-member, experiments at deep transition zone conditions produce a mixture of stishovite and wüstite, magnetite, or ringwoodite (Tateno et al. 2007; Ismailova et al. 2015). Maximum observed solubility of $FeSiO_3$ in $R\bar{3}$ $MgSiO_3$ akimotoite (green area) is based on experiments at 1100°C and 24 GPa by Ito and Yamada (1982). Natural $R\bar{3}$ hemleyite (green dot) was characterized with higher Fe^{2+}-content than the experimental solubility limit (Bindi et al. 2017). Composition of Fe^{3+}-bearing LN-type phase (blue area) coexisting with bridgmanite is obtained from experiments at 1873 K, 20-24 GPa as reported in (Wang et al. 2021). Hem50-LN (50% hematite, 50% enstatite) investigated in this study and (Chanyshev et al. 2023; Koemets et al. 2023) is represented by the blue dot.

The $R3c$ $LiNbO_3$-type or modified $R3$ corundum structure in $(Mg_{0.5}Fe_{0.5}{}^{3+})(Fe_{0.5}{}^{3+}Si_{0.5})O_3$ is inferred to result from back-transformation from bridgmanite or a related double perovskite structure on decompression from 24-27 GPa (Wang et al. 2021; Chanyshev et al. 2023; Koemets et al. 2023). The $LiNbO_3$-type structure is known to readily transform to a perovskite-type structure and back in a number of compounds (Ross et al. 1989; Funamori et al. 1997; Linton et al. 1997; Inaguma et al. 2014; Akaogi et al. 2017; Zhu et al. 2020; Koemets et al. 2023). However, the range of conditions over which Fe^{3+}-bearing bridgmanite is stable is not known. Furthermore, the separate Fe^{3+}-rich phase was also observed upon recovery from transition zone conditions of 15 GPa and 1773 K (Wang et al. 2021). This synthesis pressure is lower than the stable pressure range not only for $MgSiO_3$ bridgmanite, expected to be stable above 20-24 GPa,

but also for $MgSiO_3$ akimotoite, stable above ~18-22 GPa (Ishii et al. 2011; Kulka et al. 2020). Experimental observations could be consistent with Fe^{3+}-rich majorite garnet or stabilization of Fe^{3+}-rich $LiNbO_3$-type silicate or bridgmanite at transition zone depths. In this study, we performed powder and single-crystal X-ray diffraction (XRD) measurements on Fe^{3+}-rich $(Mg_{0.46}, Fe^{3+}_{0.53})(Si_{0.49}, Fe^{3+}_{0.51})O_3$ at ambient conditions and high pressures as well as first-principles calculations to reveal its crystal structure, compressibility, and phase transition mechanism to bridgmanite.

2 Materials and Methods

2.1 Experimental methods

Synthesis and compositional characterization of the Fe^{3+}-rich starting material used in this work is described in Liu et al. (2018) and Dorfman et al. (2020). Electron microprobe analysis shows the sample is chemically homogeneous with a composition of $Mg_{0.46(2)}Fe_{1.04(1)}Si_{0.49(1)}O_3$ (Liu et al. 2018), and conventional Mössbauer spectroscopy is consistent with 100% Fe^{3+}/total Fe (Dorfman et al. 2020). Hence, the stoichiometric chemical formula of the sample is determined to be $(Mg_{0.46}, Fe^{3+}_{0.53})(Si_{0.49}, Fe^{3+}_{0.51})O_3$. Crystals used in single-crystal diffraction measurements were ~200 × 200 × 200 μm^3, while polycrystalline aggregates with few-μm grain size were used for powder diffraction measurements.

Single-crystal X-ray diffraction (XRD) was carried out at ambient conditions at the GSECARS facility at APS, Argonne National Laboratory, in station 13BM-C. A silicon (311) monochromator was used to select X-rays at 28.6 keV (0.434 Å) with 1 eV bandwidth. Kirkpatrick-Baez mirrors focused the beam to vertical × horizontal focus spot size of 15 μm × 15 μm, measured as full width at half maximum (FWHM). The MAR165 Charge Coupled Device (CCD) detector (Rayonix) was placed about 200 mm away from the sample. LaB_6 powder standard was used to calibrate the distance and orientation of the detector. A ~200 × 200 × 200 μm^3 crystal of $(Mg_{0.46}Fe^{3+}_{0.53})(Si_{0.49},Fe^{3+}_{0.51})O_3$ was mounted onto a polymer micromesh sample holder (MiTeGen) for room pressure measurement. The sample was centered at the axis of rotation of the diffractometer and aligned with an optical microscope. At room pressure, a series of 10° wide segment rotation exposure covered angular range from φ= -90° to 90°, followed by a series of step φ-exposures, each covering 1° scan width. The typical exposure time was 1s/°. At

zero diffractometer position, the φ scan rotation axis for the 13BM-C diffractometer is in the horizontal plane of the instrument, and is perpendicular to the incident X-ray direction. The diffraction images were analyzed using the GSEADA/RSV software package (Dera et al. 2013). SHELXL software was used for refinement (Sheldrick 2015). We used isotropic atomic displacement parameters (U_{iso}) for all atoms due to the lack of independent reflections.

A symmetric diamond anvil cell (DAC) with 300-μm flat diamonds was used for high-pressure experiments at ambient temperature. A 250-μm thick rhenium gasket was pre-indented to ~30 μm, and a hole with diameter of 150 μm was drilled in the center using the laser drilling system at HPCAT (Sector 16) of the Advanced Photon Source (APS), Argonne National Laboratory (ANL) (Hrubiak et al. 2015). A polycrystalline sample aggregate sized ~20 × 20 × 7 μm^3 was loaded into the sample chamber, and then Ne was loaded as a hydrostatic pressure medium using the COMPRES/GSECARS gas-loading system (Rivers et al. 2008). Au powder was spread on top of the sample serving as pressure standard with minimal pressure gradient between sample and Au (Liu et al. 2018). Pressure was calculated from the Au (111) peak using the equation of state (Fei et al. 2007).

The crystal structure during compression in the DAC was determined by angle-dispersive synchrotron XRD measurements performed at beamline 13-BM-C of the APS, ANL with beam characteristics and detector position calibration as described above. On compression at intervals of 1-2 GPa, XRD images of the samples were recorded for an exposure time of 60 s. The XRD images were integrated using the software DIOPTAS (Prescher and Prakapenka 2015). Crystal structures were examined using full spectrum Le Bail fitting implemented in the EXPGUI/GSAS software package (Toby 2001), and the unit cell parameters were extracted based on five diffraction lines (012, 104, 110, 113, 024, 116) using the program PDIndexer (Seto et al. 2010).

2.3 First-principles calculations of the phase transition pathway

To determine the effects of compositional and structural differences between $MgSiO_3$ and $(Mg_{0.5}Fe_{0.5})(Fe_{0.5}Si_{0.5})O_3$ on the phase transition path and energy barrier for formation of bridgmanite, we performed calculations using the stochastic surface walking (SSW) method integrated with density functional theory (DFT). SSW has successfully been used to predict the low-energy pathways of crystal phase transitions (e.g., Zhu et al. 2019). Calculations employed the Vienna ab initio simulation package (VASP) for plane wave DFT. Electron-ion interactions

for all atoms were represented in VASP using the projector augmented wave (PAW) scheme. The exchange-correlation functional is described by the generalized gradient approximation in the Perdew-Burke-Ernzerhof parameterization. The pathway sampling was carried out in a 20-atom (4 $MgSiO_3$ units per cell) lattice for akimotoite, $LiNbO_3$-type phase, and bridgmanite. Through SSW sampling, a large set (~10^2) of initial/final state pairs was collected at 24 GPa. TS was located using double-ended surface walking. The lowest energy pathway was found by sorting the heights of computed energy barriers. Then, the lowest candidate pathway was refined by solid-state NEB (ssNEB) method. In order to speed up the sampling, the Monkhorst-Pack *k*-point mesh of (4×4×4) set for sampling and energy barrier scan is 2 x 2 x 2, while for barrier refinement the Monkhorst-Pack k-point mesh is set to 4 x 4 x 4. The kinetic energy plane wave cutoff is 500 eV. For all the structures, both lattice and atomic positions were fully optimized until the maximal stress component is below 0.1 GPa and the maximal force component below 0.01 eV/Å.

3 Results and discussion

3.1. $LiNbO_3$-structured $(Mg_{0.5}Fe_{0.5})(Fe_{0.5}Si_{0.5})O_3$

At ambient conditions, single crystal and powder XRD indicate that $(Mg_{0.5}Fe_{0.5})(Fe_{0.5}Si_{0.5})O_3$ recovered from synthesis at 24 GPa and 1873 K adopts the $LiNbO_3$-type structure (**Figure 2**). We attempted to fit each dataset using the $R\bar{3}$ ilmenite-type structure, *R*3*c* $LiNbO_3$-type structure, and corundum-derivative *R*3 structure proposed by (Koemets et al. 2023) based on contemporaneous experiments. The $R\bar{3}$ ilmenite-type structure and *R*3*c* differ only in the ordering of the two cation sites (Supplementary Figure S1). *R*3 is nearly identical to *R*3*c* but has lower symmetry. For the single-crystal XRD data, fits to the $R\bar{3}$ ilmenite and *R*3 structures do not converge. Additional peaks expected for the $R\bar{3}$ ilmenite structure are not present. Due to the group-subgroup relationship between the *R*3 and *R*3*c* structures, it is possible to describe the observed peaks with the *R*3 structure, and failure to converge may be due to the higher number of degrees of freedom in the fit and completeness of the dataset. The fit to the *R*3*c* $LiNbO_3$-type structure converges with R1-value of 7.11% and goodness of fit 1.423. Refinement details, fractional coordinates and atomic displacement parameters are given in Supplementary Tables S1 and S2. Powder diffraction peaks are also consistent with *R*3*c* $LiNbO_3$-type structure.

This is the peer-reviewed, final accepted version for American Mineralogist, published by the Mineralogical Society of America.
The published version is subject to change. Cite as Authors (Year) Title. American Mineralogist, in press.
DOI: https://doi.org/10.2138/am-2024-9410. http://www.minsocam.org/

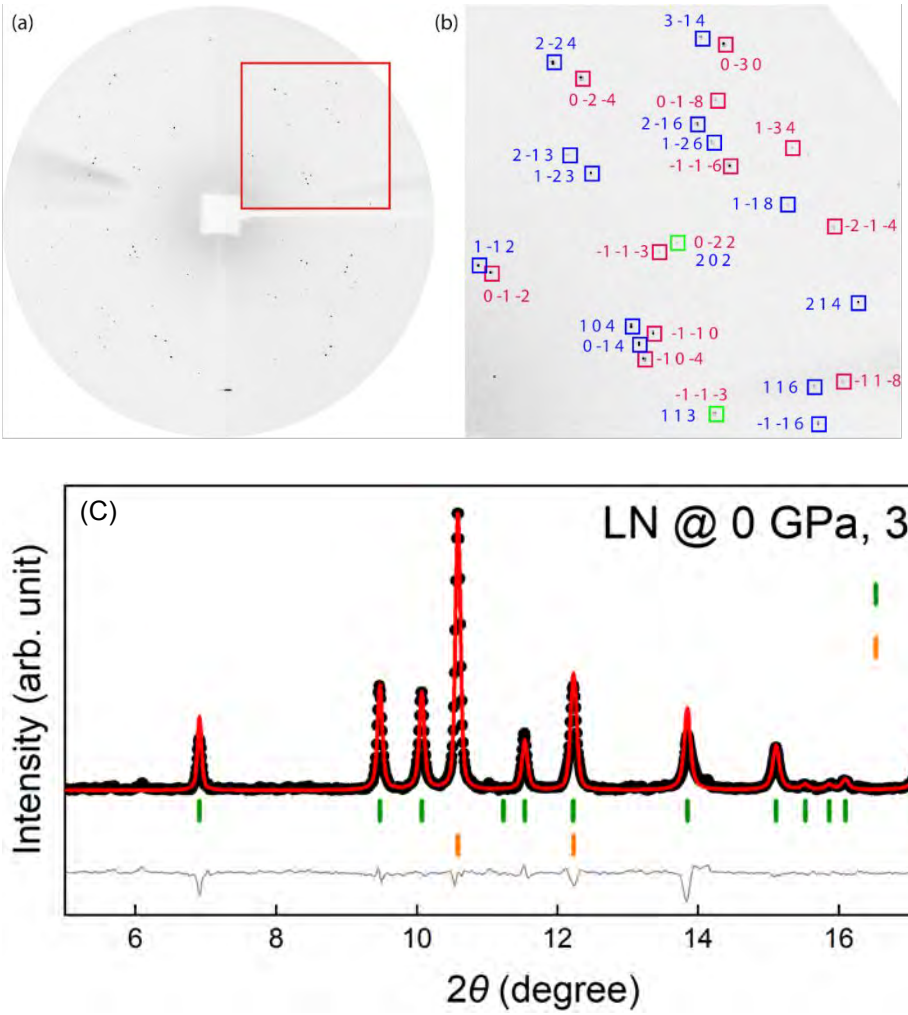

Figure 2. Single-crystal and powder diffraction observations (λ=0.434 Å) and fits for synthetic $(Mg_{0.46}Fe^{3+}_{0.53})(Si_{0.49}Fe^{3+}_{0.51})O_3$ at 0 GPa and 300 K. (a-b) Single-crystal X-ray diffraction pattern viewed along (1 0 0) direction with peaks identified corresponding to the hexagonal *R*3*c* crystal structure. The Mg/Fe and Si/Fe octahedra are represented by red and blue boxes, respectively. Unit cell parameters obtained from this fit are a=4.9496(5) and c=13.3138(19), and V=282.47(6). (c) Le Bail fitting applied to background-subtracted powder X-ray diffraction pattern: red solid curve represents the refined profile, and green and orange vertical ticks indicate the $LiNbO_3$-type structure and Au, respectively. Refined unit cell parameters are a = 4.950(5) Å, c =13.323(2) Å, and V = 282.8(6) Å^3.

The ratio of c and a lattice parameters for the $(Mg_{0.5}Fe_{0.5})(Fe_{0.5}Si_{0.5})O_3$ is also more consistent with previous observations of $LiNbO_3$-type compounds than ilmenites. Refined lattice parameters for $(Mg_{0.5}Fe_{0.5})(Fe_{0.5}Si_{0.5})O_3$ at 1 bar yield c/a ratio of 2.69 in both this study and (Koemets et al. 2023). This value is near the upper end of the 2.61–2.70 range reported for silicate, titanate, niobate, stannate, and other compounds with $LiNbO_3$-type ordering (Leinenweber et al. 1995; Linton et al. 1999; Aimi et al. 2011) and lower than the 2.74–2.94

range reported for ilmenite-type ordering (Wechsler and Prewitt 1984; Kumada et al. 1990; Baraton et al. 1994). Among ilmenite-structured silicates, $R\bar{3}$ $MgSiO_3$ akimotoite exhibits a c/a ratio of 2.87 and the ratio for $R\bar{3}$ $FeSiO_3$ hemleyite is 2.88 (Bindi et al. 2017). For Fe^{3+}- and Al^{3+}-bearing $(Mg_{0.5}Fe_{0.5})(Al_{0.5}Si_{0.5})O_3$, the c/a ratio is much lower at 2.65-2.67 and diffraction was consistent with the $LiNbO_3$-type structure (Zhu et al. 2020; Koemets et al. 2023). The charge-coupled substitution of Fe^{3+}, $Mg_A^{2+} + Si_B^{4+} = Fe_A^{3+} + Fe_B^{3+}$, distributes Fe^{3+} evenly between the AO_6 and BO_6 octahedra and effectively homogenizes these two sites. Fe^{3+}-rich silicates are thus close to the stability boundary between these two similar structures.

$LiNbO_3$-type (LN) $(Mg_{0.5}Fe_{0.5})(Fe_{0.5}Si_{0.5})O_3$ (50% hematite, 50% enstatite, called Hem50 hereafter) diffraction peaks are observed from 1 bar to 18.3(1) GPa at 300 K. XRD patterns of sample assemblages showed diffraction peaks from Hem50-LN, Au calibrant, and Ne medium (Supplementary Fig. S2). We observe no evidence of peak splitting, broadening, dissociation or transition of the LN structure up to 18.3(1) GPa.

3.2. Equation of state

The compression properties of Hem50-LN were obtained based on volumetric compression measurements from 0 to 18.3(1) GPa (Supplementary Table S3, Figure 3). Pressure-volume (P-V) data for Hem50-LN were fit to a 2nd-order Birch-Murnaghan equation of state (BM-EoS). Resulting parameters are listed with literature values in Supplementary Table S4. The slope of normalized stress-Eulerian strain (F-f) fitting is flat (Supplementary Figure S3), supporting the validity of fixing K_0' to 4. The V_0 for Hem50- LN is consistent with 50% linear mixing between that of $MgSiO_3$ akimotoite (Wang et al. 2004) and Fe_2O_3 hematite (Bykova et al. 2016), although the crystal structures of the end-members are different. Observed volumes are consistent with measurements obtained by Koemets et al. (2023), although they do not report equation of state for the modified corundum structure for this composition. K_0 and K_0' of $MgSiO_3$ akimotoite have recently been constrained by Brillouin spectroscopy, ultrasonic, powder XRD measurements (Wang et al. 2004; Zhou et al. 2014; Siersch et al. 2021) and theoretical calculations (Hao et al. 2019) to range between 205-210 GPa and 4.2-4.8, respectively. Comparison between Hem50-LN and $MgSiO_3$ akimotoite indicates incorporation of Fe^{3+} through substitution of $(Mg^{2+}+Si^{4+})$ on both A-site and B-site decreases the incompressibility of $MgSiO_3$ akimotoite (Figure 3). The equation of state parameters of $FeSiO_3$ akimotoite compiled by

Stixrude and Lithgow-Bertelloni (2012) show a similar increase in K_0 compared to due to incorporation of Fe^{2+} on A-site.

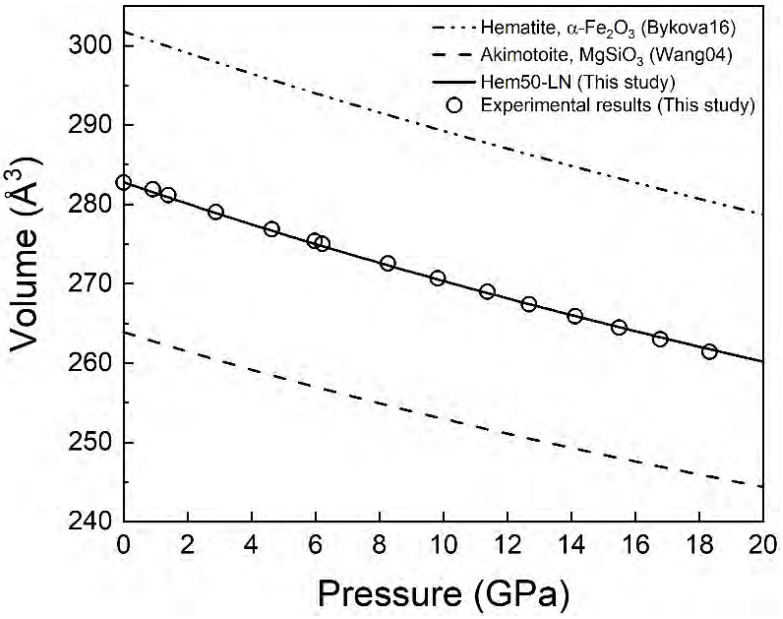

Figure 3. *P-V* plot for Hem50-LN, $MgSiO_3$ akimotoite (Wang et al. 2004), and Fe_2O_3 hematite (Bykova et al. 2016).

3.3. Transition to perovskite-type structure

At pressures higher than 18.3 GPa, new peaks corresponding to orthorhombic bridgmanite (space group *Pnma*, hereafter Hem50-Bdg) gradually replace Hem50-LN (Figure 4). Clear signatures of the transition include the disappearance of the Hem50-LN (104) peak at 2θ around 9.7° and increasing intensity of the Hem50-Bdg (112) peak at 2θ around 10.1° (Figure 4). The Hem50-LN to Hem50-Bdg polymorphic transition was completed at 24.7(1) GPa. Full-profile Le Bail refinement of XRD pattern at 18.3 compared to the pattern at 24.7 GPa confirms the Hem50 LN-to-Bdg transition and pressure range. In conjunction with previous reported 300 K equation of state parameters of Hem50-Bdg, $MgSiO_3$ Aki and Bdg, we can calculate that the unit-cell volume decreases 3.5% across Hem50-LN to Bdg transition at 20 GPa. This contrast is relatively smaller than the volume contrast of 5.9% across $MgSiO_3$ Aki and Bdg transition at 24 GPa.

This is the peer-reviewed, final accepted version for American Mineralogist, published by the Mineralogical Society of America.
The published version is subject to change. Cite as Authors (Year) Title. American Mineralogist, in press.
DOI: https://doi.org/10.2138/am-2024-9410. http://www.minsocam.org/

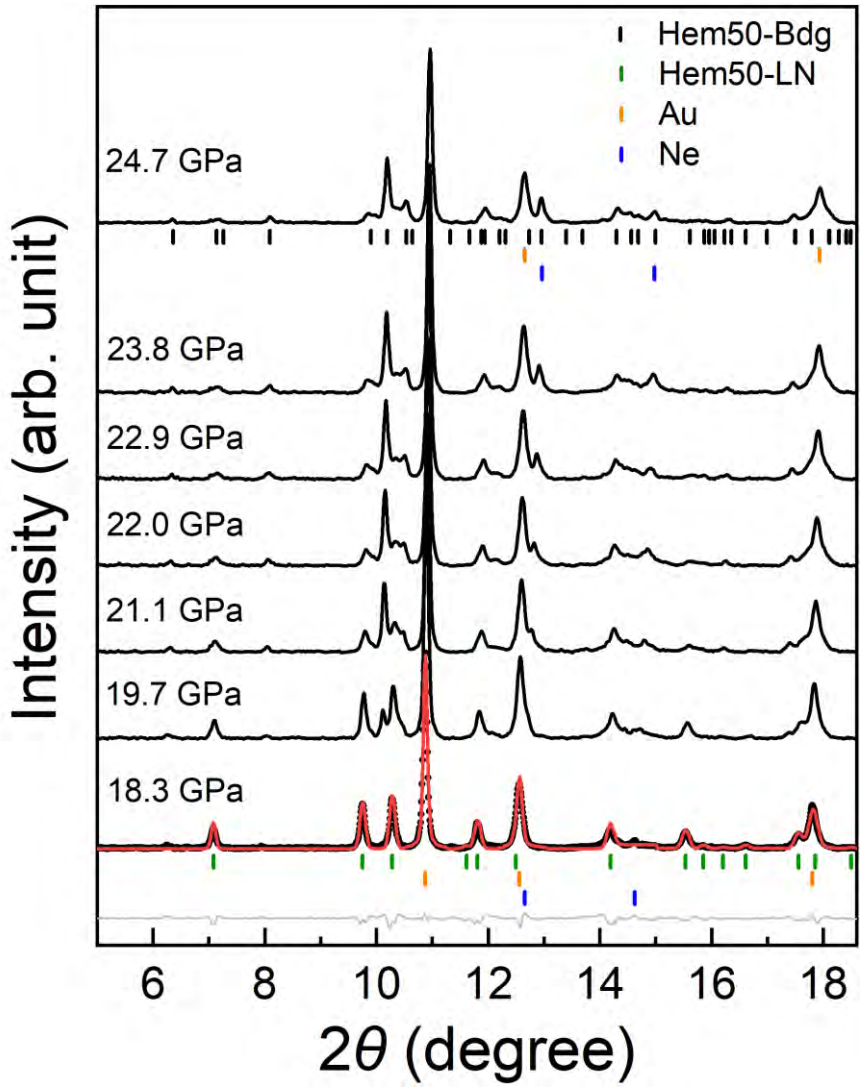

Figure 4. Representative powder X-ray diffraction patterns of $(Mg_{0.46},Fe^{3+}_{0.53})(Si_{0.49}, Fe^{3+}_{0.51})O_3$ at 18.3 - 24.7 GPa and 300 K, which show a phase transition from $LiNbO_3$-type structure to bridgmanite. Le Bail fitting is applied to interpret the pattern at 18.3 GPa: The red solid curve represents the refined profile, the gray curve represents misfit, and the vertical ticks represent $LiNbO_3$-type structure (green), Au (orange) and Ne (blue), respectively. At 24.7 GPa, the vertical ticks represent bridgmanite (black), Au (orange) and Ne (blue). The wavelength of the incident X-ray beam is 0.434 Å.

The transition from Hem50-LN to Hem50-Bdg occurred at 300 K without heating, which implies a low kinetic barrier between the two Fe^{3+}-rich phases along the $MgSiO_3$-Fe_2O_3 join. In contrast to the observed low kinetic energy barrier between Hem50-LN to Hem50-Bdg, the $MgSiO_3$ Aki – Bdg transition has been documented to require high temperature to overcome a high energy barrier (Ono et al. 2001). However, the $LiNbO_3$-type structure transforms to orthorhombic perovskite at room temperature on compression and the reverse on decompression for several compositions including $(Mg,Mn,Fe,Zn)TiO_3$ (Ross et al. 1989; Linton et al. 1997;

Inaguma et al. 2014; Akaogi et al. 2017), $(Mg_{0.37}Fe_{0.22}Ca_{0.16}Mn_{0.01}Al_{0.25})(Al_{0.25}Si_{0.75})O_3$ (Funamori et al. 1997), and $(Mg_{0.5},Fe^{3+}_{0.5}))(Si_{0.5}, Al^{3+}_{0.5})O_3$ (Zhu et al. 2020; Koemets et al. 2023). The favorable kinetics of this transition is attributed to the ordering of cations in the $LiNbO_3$-type structure that matches the perovskite ordering (Ross et al. 1989) and further promoted by interchangeable ions on both cation sites. The octahedral (Fe^{3+}, Si) site can rotate to form the BO_6 octahedral network of the perovskite structure without breaking bonds (Megaw 1968). In addition, for $(Mg_{0.5},Fe^{3+}_{0.5})(Si_{0.5}, Fe^{3+}_{0.5})O_3$ LN, Fe^{3+} ions in either A or B sites can become Fe^{3+} in either A or B sites in $(Mg_{0.5},Fe^{3+}_{0.5}))(Si_{0.5}, Fe^{3+}_{0.5})O_3$-bridgmanite, facilitating rearrangement of sites without diffusing atoms during the phase transition. Thus, $MgSiO_3$ akimotoite and $(Mg_{0.5},Fe^{3+}_{0.5})(Si_{0.5}, Fe^{3+}_{0.5})O_3$ LN have different atom-to-atom correspondence pathways, and consequently, more energy is needed to transform the akimotoite to correctly A/B sorted bridgmanite.

We confirm the phase transition mechanism of Hem50-LN to Hem50-Bdg and the effects of incorporation of Fe^{3+} on the energy barrier via theoretical simulations. We investigated the structural transformation between Hem50-LN to Hem50-Bdg and $MgSiO_3$ Aki to Bdg, and identified their lowest energy pathways, respectively (Figure 5). The mechanism of the transformation between these related structures (Figure S1) is octahedral tilting. The enthalpy barrier of the Hem50-LN to Hem50-Bdg transition is 0.19 eV/formula unit (f.u.) (18.33 KJ/mol), which is only 14% of the 1.36 eV/f.u (131.22 KJ/mol) barrier for Fe-free Aki to Bdg transition. The low enthalpy barrier between Hem50-LN to Hem50-Bdg explains our observation that the transition thus can proceed even at ambient temperature. As a comparison, the activation energy for post-spinel transformation in Mg_2SiO_4 was estimated as 355 KJ/mol (Kubo et al. 2002a), which requires overpressure of more than ~1 GPa at the transformation at 700 km depth in cold slabs. Growth of majoritic garnet (van Mierlo et al. 2013) and transformation from garnet to bridgmanite (Kubo et al. 2002b) have also been argued to be delayed by kinetics in cold slabs. In contrast, the ilmenite/ $LiNbO_3$-type structure to Bdg transition would be more kinetically-favorable than the post-spinel or post-garnet transition.

This is the peer-reviewed, final accepted version for American Mineralogist, published by the Mineralogical Society of America.
The published version is subject to change. Cite as Authors (Year) Title. American Mineralogist, in press.
DOI: https://doi.org/10.2138/am-2024-9410. http://www.minsocam.org/

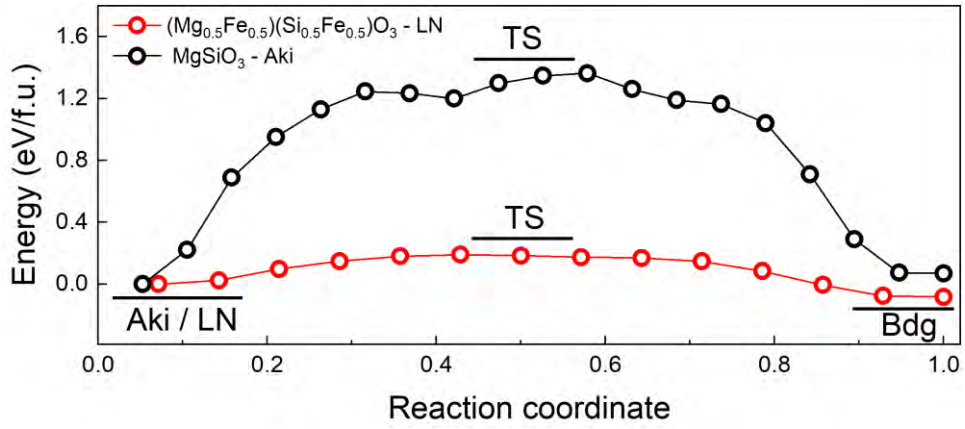

Figure 5. Potential energy profile connecting $(Mg_{0.5},Fe^{3+}_{0.5})(Si_{0.5}, Fe^{3+}_{0.5})O_3$ $LiNbO_3$-type structure and bridgmanite (red dot line) compared to $MgSiO_3$ akimotoite and bridgmanite (black dot line), obtained by first-principles free-energy landscape sampling methods. A transition state (TS) can be located among the pathway.

The transition from LN-type phase to Bdg observed for our Fe^{3+}-rich composition started on compression between 18.3-19.7 GPa at 300 K. The onset of the transition is similar to the 18 GPa transition observed for LN-type $(Mg_{0.5},Fe^{3+}_{0.5})(Si_{0.5},Al_{0.5})O_3$ powder (Zhu et al. 2020). However, experiments on single crystals of LN-type $(Mg_{0.5},Fe^{3+}_{0.5})(Si_{0.5},Al_{0.5})O_3$ and modified corundum *R*3 structure of $(Mg_{0.5},Fe^{3+}_{0.5})(Si_{0.5}, Fe^{3+}_{0.5})O_3$ indicate transitions to Bdg or a novel double perovskite at lower pressures, 8(2) and 12(2) GPa respectively (Koemets et al. 2023). The difference in the observed transition pressures could be due to structure/compositional difference between the samples or differences in stress conditions in single crystal vs. powder (although all studies employed neon quasi-hydrostatic pressure-transmitting medium). This difference in transition conditions could also indicate the metastability of the LN-type phase. If hysteresis is observed in the transition, the conditions at which the Gibbs free energy of the bridgmanite phase becomes lower than the LN-type phase, whether or not this is the minimum energy (equilibrium) state, should be between the minimum observed transition pressure on compression and maximum transition pressure on decompression.

If 12(2) GPa is an upper bound on the LN or modified corundum *R*3 structure to (single or double) perovskite transition, this would be consistent with crystallization as perovskite-type phase at 15-27 GPa in all experiments by Wang et al. (2021), Chanyshev et al. (2023), and Koemets et al. (2023) and transformation to the *R*3c or *R*3 structure on decompression. These studies do not have in-situ characterization to confirm the structure formed at 15-27 GPa. Because synthesis experiments performed in the bridgmanite stability field yielded $LiNbO_3$-type

phase upon quenching to ambient pressures, we infer that the reverse transition during decompression proceeds without heating as well (Liu et al. 2018; Wang et al. 2021). In addition, if the Clapeyron slope of the conditions of the LN-Bdg transition is negative (like the Aki-Bdg transition), the LN-Bdg transition could occur at even lower pressures at high temperatures. These results point to Fe^{3+} stabilizing the perovskite structure within the Earth's transition zone.

4 Geophysical implications

Differences in the stability of corundum-family and bridgmanite structures due to composition may impact the dynamics of subducting slabs. $MgSiO_3$ akimotoite in subducting slabs is thought to impede subduction at 660 km depth due to the Aki-Bdg transition with a negative Clapeyron slope and low density (e.g. Chanyshev et al. 2022). Incorporation of up to ~10% $Fe^{2+}SiO_3$ in ilmenite-structured akimotoite was observed to have no effect on the transition from akimotoite to bridgmanite, or possibly slightly increase the transition pressure based on observed compositions of coexisting phases (Ito and Yamada 1982), further impeding subduction. In contrast, in an oxidized Fe-bearing system, dense Fe^{3+}-bearing bridgmanite may be stable within the $MgSiO_3$ akimotoite stability field. Crystallization of this dense phase within oxidized subducting lithosphere at transition zone pressures may facilitate subduction.

Whether phase transitions from akimotoite or spinel to bridgmanite result in a seismic discontinuity depends on the depth range of coexistence of low-pressure and high-pressure phase. Incorporation of Al in $MgSiO_3$ bridgmanite is predicted to broaden the transition pressure range by ~1 GPa, and increase the Aki-Bdg transition pressure by ~2-3 GPa along a cold slab geotherm (Ita and Stixrude 1992; Vacher et al. 1998; Akaogi et al. 2002). For compositions enriched in Al^{3+}, this breadth suggests that a transition from the Aki to Bdg would not be observable globally as a sharp seismic discontinuity. The 660-km discontinuity can be explained by the post-spinel transition in both pyrolite (Ishii et al. 2011) and harzburgite (Irifune and Ringwood 1987) not only due to its steep Clapeyron slope, but also the extremely narrow transition pressure interval (Ito and Takahashi 1989; Ishii et al. 2019). In the $MgSiO_3$-Fe_2O_3 system investigated by (Wang et al. 2021; Chanyshev et al. 2023), most of the Fe_2O_3 component partitions into the Fe^{3+}-rich phase, leaving relatively Fe^{3+}-depleted spinel and bridgmanite. This partitioning can be expected to further sharpen the post-spinel phase boundary at 660 km. Because the $LiNbO_3$-type phase does not appear to be stable and bridgmanite would replace

akimotoite, no discontinuity would be observed associated with the akimotoite-bridgmanite transition in oxidized Fe-bearing mantle.

The stability of Fe^{3+}-rich bridgmanite in the transition zone depends on the presence of sufficient iron and high oxygen fugacity. Mantle lithologies exhibit widely ranging oxygen fugacity (Cottrell et al. 2021), and upwelling plumes also may be relatively oxidized (Moussallam et al. 2019). Self-disproportionation of Fe^{2+} may elevate the concentration of Fe^{3+} in the transition zone, as in the lower mantle for the mineral bridgmanite (Frost et al. 2004; Rohrbach et al. 2007; Chanyshev et al. 2023). As a minor phase, Fe^{3+}-bearing bridgmanite in the transition zone would not dominate seismic properties, but could have a significant effect on density, composition, and seismic properties of the overall phase assemblage.

The $LiNbO_3$-type structure has also been observed in natural materials that have been shocked to high pressures during planetary impacts and inferred to represent back-transformation from the perovskite structure. $LiNbO_3$-structured $FeTiO_3$, now named wangdaoite, was documented in the Ries impact crater (Dubrovinsky et al. 2009) and in the Suizhou chondritic meteorite (Xie et al. 2020). In these samples, coexisting minerals suggest shock pressures estimated in the range 16-28 GPa, corresponding to the $FeTiO_3$ perovskite stability field. Shock veins in chondrites also contain $R\bar{3}$ $FeSiO_3$ hemleyite (Bindi et al. 2017) and $MgSiO_3$ akimotoite (Tschauner et al. 2018) and *Pnma* $FeSiO_3$ hiroseite (Bindi et al. 2020) and $MgSiO_3$ bridgmanite (Tschauner et al. 2014). In contrast to natural hemleyite, which was reported to contain no significant ferric iron, natural hiroseite was observed with Fe^{3+}/Fe total ~19%, supporting the importance of crystal chemistry of Fe^{3+} in perovskites. However, interpretation of $R\bar{3}c$ hematite in meteorites is complicated by the many mechanisms by which this phase forms, including weathering and low-pressure, high-temperature decomposition of silicates (e.g. Kuchka et al. 2017). The results of this work provide constraints on interpreting intermediate $MgSiO_3$-Fe_2O_3 phases transformed during shock impacts.

5 Conclusions

We performed high-pressure XRD measurements on synthetic $LiNbO_3$-type $(Mg_{0.46},Fe^{3+}_{0.53})(Si_{0.49}, Fe^{3+}_{0.51})O_3$ (Hem50-LN), and we observed the Hem50-LN to Bdg transition occurring between 18.3 GPa -24.7 GPa at 300 K. We investigated the phase transition mechanism of akimotoite and $LiNbO_3$-structured phases to bridgmanite with compositions of

both $MgSiO_3$ and $(Mg_{0.5},Fe^{3+}_{0.5})(Si_{0.5}, Fe^{3+}_{0.5})O_3$ via first-principles calculation and determined that accommodating Fe in LN-phase results in a lowered kinetic energy to transform to bridgmanite relative to transforming to bridgmanite from akimotoite. Our experiments and calculations confirm that accommodating Fe^{3+} in LN can significantly decrease the kinetic energy barrier to crystallize bridgmanite. Due to enrichment of Fe^{3+}, this dense phase may play an important role in slab dynamics and localized geochemical anomalies.

Acknowledgments

The experimental work was supported by NSF grants (EAR-1664332, EAR-1751664) to S. Dorfman. Portions of this work were performed at GeoSoilEnviroCARS (The University of Chicago, Sector 13), Advanced Photon Source (APS), Argonne National Laboratory. GeoSoilEnviroCARS is supported by the National Science Foundation – Earth Sciences (EAR – 1634415). This research used resources of the Advanced Photon Source, a U.S. Department of Energy (DOE) Office of Science User Facility operated for the DOE Office of Science by Argonne National Laboratory under Contract No. DE-AC02-06CH11357. Use of the COMPRES-GSECARS gas loading system was supported by COMPRES under NSF Cooperative Agreement EAR -1606856 and by GSECARS through NSF grant EAR-1634415 and DOE grant DE-FG02-94ER14466. This research used resources of the Advanced Photon Source, a U.S. Department of Energy (DOE) Office of Science User Facility operated for the DOE Office of Science by Argonne National Laboratory under Contract No. DE-AC02-06CH11357. S.C. Zhu is supported by Fundamental Research Funds for the Central Universities, Sun Yat-sen University, No.23qnpy04. Li acknowledges support from NSF EAR2310830. F. Zhu acknowledges support from National Natural Science Foundation of China (NSFC) grant (no. 42102035). X. Lai acknowledges support from NSFC grant (no. 42372054).

References

Aimi, A., Katsumata, T., Mori, D., Fu, D., Itoh, M., Kyômen, T., Hiraki, K., Takahashi, T., and Inaguma, Y. (2011) High-Pressure Synthesis and Correlation between Structure, Magnetic, and Dielectric Properties in LiNbO3-Type MnMO3 (M = Ti, Sn). Inorganic Chemistry, 50, 6392–6398.

Akaogi, M., Tanaka, A., and Ito, E. (2002) Garnet–ilmenite–perovskite transitions in the system Mg4Si4O12–Mg3Al2Si3O12 at high pressures and high temperatures: phase equilibria, calorimetry and implications for mantle structure. Physics of the Earth and Planetary Interiors, 132, 303–324.

Akaogi, M., Abe, K., Yusa, H., Ishii, T., Tajima, T., Kojitani, H., Mori, D., and Inaguma, Y. (2017) High-pressure high-temperature phase relations in FeTiO3 up to 35 GPa and 1600 °C. Physics and Chemistry of Minerals, 44, 63–73.

Baraton, M.I., Busca, G., Prieto, M.C., Ricchiardi, G., and Escribano, V.S. (1994) On the Vibrational Spectra and Structure of FeCrO3 and of the Ilmenite-Type Compounds CoTiO3 and NiTiO3. Journal of Solid State Chemistry, 112, 9–14.

Bindi, L., Chen, M., and Xie, X. (2017) Discovery of the Fe-analogue of akimotoite in the shocked Suizhou L6 chondrite. Scientific Reports, 7, 42674.

Bindi, L., Shim, S.-H., Sharp, T.G., and Xie, X. (2020) Evidence for the charge disproportionation of iron in extraterrestrial bridgmanite. Science Advances, 6, eaay7893.

Bykova, E., Dubrovinsky, L., Dubrovinskaia, N., Bykov, M., McCammon, C., Ovsyannikov, S.V., Liermann, H.-P., Kupenko, I., Chumakov, A.I., Rüffer, R., and others (2016) Structural complexity of simple Fe_2O_3 at high pressures and temperatures. Nature Communications, 7, ncomms10661.

Chanyshev, A., Ishii, T., Bondar, D., Bhat, S., Kim, E.J., Farla, R., Nishida, K., Liu, Z., Wang, L., Nakajima, A., and others (2022) Depressed 660-km discontinuity caused by akimotoite–bridgmanite transition. Nature, 601, 69–73.

Chanyshev, A., Fei, H., Bondar, D., Wang, B., Liu, Z., Ishii, T., Farla, R., McCammon, C., and Katsura, T. (2023) Ferric Iron Substitution Mechanism in Bridgmanite under SiO2-Saturated Conditions at 27 GPa. ACS Earth and Space Chemistry, 7, 471–478.

Cottrell, E., and Kelley, K.A. (2011) The oxidation state of Fe in MORB glasses and the oxygen fugacity of the upper mantle. Earth and Planetary Science Letters, 305, 270–282.

Cottrell, E., and Kelley, K.A. (2013) Redox Heterogeneity in Mid-Ocean Ridge Basalts as a Function of Mantle Source. Science, 340, 1314–1317.

Cottrell, E., Birner, S.K., Brounce, M., Davis, F.A., Waters, L.E., and Kelley, K.A. (2021) Oxygen Fugacity Across Tectonic Settings. In Magma Redox Geochemistry pp. 33–61. American Geophysical Union (AGU).

Dera, P., Zhuravlev, K., Prakapenka, V., Rivers, M.L., Finkelstein, G.J., Grubor-Urosevic, O., Tschauner, O., Clark, S.M., and Downs, R.T. (2013) High pressure single-crystal micro X-ray diffraction analysis with GSE_ADA/RSV software. High Pressure Research, 33, 466–484.

Dorfman, S.M., Potapkin, V., Lv, M., Greenberg, E., Kupenko, I., Chumakov, A.I., Bi, W., Alp, E.E., Liu, J., Magrez, A., and others (2020) Effects of composition and pressure on electronic states of iron in bridgmanite. American Mineralogist, 105, 1030–1039.

Dubrovinsky, L.S., El Goresy, A., Gillet, Ph., Wu, X., and Simionivici, A. (2009) A Novel Natural Shock-induced High-Pressure Polymorph of FeTiO3 with the Li-Niobate Structure from the Ries Crater, Germany. Meteoritics and Planetary Science Supplement, 72, 5094.

Faccenda, M., and Dal Zilio, L. (2017) The role of solid–solid phase transitions in mantle convection. Lithos, 268–271, 198–224.

Fei, Y., Ricolleau, A., Frank, M., Mibe, K., Shen, G., and Prakapenka, V.B. (2007) Toward an internally consistent pressure scale. Proceedings of the National Academy of Sciences, 104, 9182–9186.

Frost, D.J., Liebske, C., Langenhorst, F., McCammon, C.A., Trønnes, R.G., and Rubie, D.C. (2004) Experimental evidence for the existence of iron-rich metal in the Earth's lower mantle. Nature, 428, 409–412.

Funamori, N., Yagi, T., Miyajima, N., and Fujino, K. (1997) Transformation in Garnet from Orthorhombic Perovskite to $LiNbO_3$ Phase on Release of Pressure. Science, 275, 513–515.

Gu, T., Li, M., McCammon, C., and Lee, K.K.M. (2016) Redox-induced lower mantle density contrast and effect on mantle structure and primitive oxygen. Nature Geoscience, 9, 723–727.

Hao, S., Wang, W., Qian, W., and Wu, Z. (2019) Elasticity of akimotoite under the mantle conditions: Implications for multiple discontinuities and seismic anisotropies at the depth of ~600–750 km in subduction zones. Earth and Planetary Science Letters, 528, 115830.

Hrubiak, R., Sinogeikin, S., Rod, E., and Shen, G. (2015) The laser micro-machining system for diamond anvil cell experiments and general precision machining applications at the High Pressure Collaborative Access Team. Review of Scientific Instruments, 86, 072202.

Inaguma, Y., Aimi, A., Shirako, Y., Sakurai, D., Mori, D., Kojitani, H., Akaogi, M., and Nakayama, M. (2014) High-Pressure Synthesis, Crystal Structure, and Phase Stability Relations of a LiNbO3-Type Polar Titanate ZnTiO3 and Its Reinforced Polarity by the Second-Order Jahn–Teller Effect. Journal of the American Chemical Society, 136, 2748–2756.

Irifune, T., and Ringwood, A.E. (1987) Phase transformations in a harzburgite composition to 26 GPa: implications for dynamical behaviour of the subducting slab. Earth and Planetary Science Letters, 86, 365–376.

Ishii, T., Kojitani, H., and Akaogi, M. (2011) Post-spinel transitions in pyrolite and Mg2SiO4 and akimotoite–perovskite transition in MgSiO3: Precise comparison by high-pressure high-temperature experiments with multi-sample cell technique. Earth and Planetary Science Letters, 309, 185–197.

Ishii, T., Huang, R., Myhill, R., Fei, H., Koemets, I., Liu, Z., Maeda, F., Yuan, L., Wang, L., Druzhbin, D., and others (2019) Sharp 660-km discontinuity controlled by extremely narrow binary post-spinel transition. Nature Geoscience, 12, 869–872.

Ismailova, L., Bobrov, A., Bykov, M., Bykova, E., Cerantola, V., Kantor, I., Kupenko, I., McCammon, C., Dyadkin, V., Chernyshov, D., and others (2015) High-pressure synthesis of skiagite-majorite garnet and investigation of its crystal structure. American Mineralogist, 100, 2650–2654.

Ita, J., and Stixrude, L. (1992) Petrology, elasticity, and composition of the mantle transition zone. Journal of Geophysical Research, 97, 6849–6866.

Ito, E., and Takahashi, E. (1989) Postspinel transformations in the system Mg2SiO4-Fe2SiO4 and some geophysical implications. Journal of Geophysical Research: Solid Earth, 94, 10637–10646.

Ito, E., and Yamada, H. (1982) Stability relations of silicate spinels, ilmenites, and perovskites. High-pressure research in geophysics, 405–419.

Ko, J., and Prewitt, C.T. (1988) High-pressure phase transition in MnTiO3 from the ilmenite to the LiNbO3 structure. Physics and Chemistry of Minerals, 15, 355–362.

Koemets, I., Wang, B., Koemets, E., Ishii, T., Liu, Z., McCammon, C., Chanyshev, A., Katsura, T., Hanfland, M., Chumakov, A., and others (2023) Crystal chemistry and compressibility of Fe0.5Mg0.5Al0.5Si0.5O3 and FeMg0.5Si0.5O3 silicate perovskites at pressures up to 95 GPa. Frontiers in Chemistry, 11, 1258389.

Kubo, T., Ohtani, E., Kato, T., Urakawa, S., Suzuki, A., Kanbe, Y., Funakoshi, K.-I., Utsumi, W., Kikegawa, T., and Fujino, K. (2002a) Mechanisms and kinetics of the post-spinel transformation in Mg2SiO4. Physics of the Earth and Planetary Interiors, 129, 153–171.

Kubo, T., Ohtani, E., Kondo, T., Kato, T., Toma, M., Hosoya, T., Sano, A., Kikegawa, T., and Nagase, T. (2002b) Metastable garnet in oceanic crust at the top of the lower mantle. Nature, 420, 803–806.

Kuchka, C.R., Herd, C.D.K., Walton, E.L., Guan, Y., and Liu, Y. (2017) Martian low-temperature alteration materials in shock-melt pockets in Tissint: Constraints on their preservation in shergottite meteorites. Geochimica et Cosmochimica Acta, 210, 228–246.

Kulka, B.L., Dolinschi, J.D., Leinenweber, K.D., Prakapenka, V.B., and Shim, S.-H. (2020) The Bridgmanite–Akimotoite–Majorite Triple Point Determined in Large Volume Press and Laser-Heated Diamond Anvil Cell. Minerals, 10, 67.

Kumada, N., Kinomura, N., and Muto, F. (1990) Crystal Structures of Ilmenite Type $LiNbO_3$ and $NaNbO_3$. Journal of the Ceramic Society of Japan, 98, 384–388.

Leinenweber, K., Linton, J., Navrotsky, A., Fei, Y., and Parise, J.B. (1995) High-pressure perovskites on the join CaTiO3-FeTiO3. Physics and Chemistry of Minerals, 22, 251–258.

Linton, J.A., Fei, Y., and Navrotsky, A. (1997) Complete Fe-Mg solid solution in lithium niobate and perovskite structures in titanates at high pressures and temperatures. American Mineralogist, 82, 639–642.

——— (1999) The MgTiO 3 -FeTiO 3 join at high pressure and temperature. American Mineralogist, 84, 1595–1603.

Liu, J., Dorfman, S.M., Zhu, F., Li, J., Wang, Y., Zhang, D., Xiao, Y., Bi, W., and Alp, E.E. (2018) Valence and spin states of iron are invisible in Earth's lower mantle. Nature Communications, 9, 1284.

Liu, Z., Dubrovinsky, L., McCammon, C., Ovsyannikov, S.V., Koemets, I., Chen, L., Cui, Q., Su, N., Cheng, J., Cui, T., and others (2019) A new (Mg0.5Fe0.53+)(Si0.5Al0.53+)O3 LiNbO3-type phase synthesized at lower mantle conditions. American Mineralogist, 104, 1213–1216.

Megaw, H.D. (1968) A note on the structure of lithium niobate, LiNbO3. Acta Crystallographica Section A, 24, 583–588.

Moussallam, Y., Longpré, M.-A., McCammon, C., Gomez-Ulla, A., Rose-Koga, E.F., Scaillet, B., Peters, N., Gennaro, E., Paris, R., and Oppenheimer, C. (2019) Mantle plumes are oxidised. Earth and Planetary Science Letters, 527, 115798.

Navrotsky, A. (1998) Energetics and Crystal Chemical Systematics among Ilmenite, Lithium Niobate, and Perovskite Structures. Chemistry of Materials, 10, 2787–2793.

Ono, S., Katsura, T., Ito, E., Kanzaki, M., Yoneda, A., Walter, M.J., Urakawa, S., Utsumi, W., and Funakoshi, K. (2001) In situ Observation of ilmenite-perovskite phase transition in MgSiO3 using synchrotron radiation. Geophysical Research Letters, 28, 835–838.

Prescher, C., and Prakapenka, V.B. (2015) DIOPTAS: a program for reduction of two-dimensional X-ray diffraction data and data exploration. High Pressure Research, 35, 223–230.

Rivers, M., Prakapenka, V., Kubo, A., Pullins, C., Holl, C.M., and Jacobsen, S.D. (2008) The COMPRES/GSECARS gas-loading system for diamond anvil cells at the Advanced Photon Source. High Pressure Research, 28, 273–292.

Rohrbach, A., Ballhaus, C., Golla–Schindler, U., Ulmer, P., Kamenetsky, V.S., and Kuzmin, D.V. (2007) Metal saturation in the upper mantle. Nature, 449, 456–458.

Ross, N.L., Ko, J., and Prewitt, C.T. (1989) A new phase transition in MnTiO3: LiNbO3-perovskite structure. Physics and Chemistry of Minerals, 16, 621–629.

Seto, Y., Nishio-Hamane, D., Nagai, T., and Sata, N. (2010) Development of a software suite on X-ray diffraction experiments. The Review of High Pressure Science and Technology, 20, 269–276.

Sharp, T.G., Lingemann, C.M., Dupas, C., and Stöffler, D. (1997) Natural Occurrence of MgSiO3-Ilmenite and Evidence for MgSiO3-Perovskite in a Shocked L Chondrite. Science, 277, 352–355.

Sheldrick, G.M. (2015) Crystal structure refinement with SHELXL. Acta Crystallographica Section C: Structural Chemistry, 71, 3–8.

Siersch, N.C., Kurnosov, A., Criniti, G., Ishii, T., Ballaran, T.B., and Frost, D.J. (2021) The elastic properties and anisotropic behavior of MgSiO3 akimotoite at transition zone pressures. Physics of the Earth and Planetary Interiors, 106786.

Stixrude, L., and Lithgow-Bertelloni, C. (2012) Geophysics of Chemical Heterogeneity in the Mantle. Annual Review of Earth and Planetary Sciences, 40.

Tateno, S., Hirose, K., Sata, N., and Ohishi, Y. (2007) Solubility of FeO in $(Mg,Fe)SiO_3$ perovskite and the post-perovskite phase transition. Physics of the Earth and Planetary Interiors, 160, 319–325.

Toby, B.H. (2001) EXPGUI, a graphical user interface for GSAS. Journal of Applied Crystallography, 34, 210–213.

Tomioka, N., and Fujino, K. (1997) Natural (Mg,Fe)SiO3-Ilmenite and -Perovskite in the Tenham Meteorite. Science, 277, 1084–1086.

Tschauner, O., Ma, C., Beckett, J.R., Prescher, C., Prakapenka, V.B., and Rossman, G.R. (2014) Discovery of bridgmanite, the most abundant mineral in Earth, in a shocked meteorite. Science, 346, 1100–1102.

Tschauner, O., Ma, C., Prescher, C., and Prakapenka, V.B. (2018) Structure analysis and conditions of formation of akimotoite in the Tenham chondrite. Meteoritics & Planetary Science, 53, 62–74.

Vacher, P., Mocquet, A., and Sotin, C. (1998) Computation of seismic profiles from mineral physics: the importance of the non-olivine components for explaining the 660 km depth discontinuity. Physics of the Earth and Planetary Interiors, 106, 275–298.

van Mierlo, W.L., Langenhorst, F., Frost, D.J., and Rubie, D.C. (2013) Stagnation of subducting slabs in the transition zone due to slow diffusion in majoritic garnet. Nature Geoscience, 6, 400–403.

Wang, W., Liu, J., Zhu, F., Li, M., Dorfman, S.M., Li, J., and Wu, Z. (2021) Formation of large low shear velocity provinces through the decomposition of oxidized mantle. Nature Communications, 12, 1911.

Wang, Y., Uchida, T., Zhang, J., Rivers, M.L., and Sutton, S.R. (2004) Thermal equation of state of akimotoite MgSiO3 and effects of the akimotoite–garnet transformation on seismic structure near the 660 km discontinuity. Physics of the Earth and Planetary Interiors, 143–144, 57–80.

Wechsler, B.A., and Prewitt, C.T. (1984) Crystal structure of ilmenite (FeTiO3) at high temperature and at high pressure. American Mineralogist, 69, 176–185.

Xie, X., Gu, X., Yang, H., Chen, M., and Li, K. (2020) Wangdaodeite, the LiNbO3-structured high-pressure polymorph of ilmenite, a new mineral from the Suizhou L6 chondrite. Meteoritics & Planetary Science, 55, 184–192.

Zhou, C., Gréaux, S., Nishiyama, N., Irifune, T., and Higo, Y. (2014) Sound velocities measurement on MgSiO3 akimotoite at high pressures and high temperatures with simultaneous in situ X-ray diffraction and ultrasonic study. Physics of the Earth and Planetary Interiors, 228, 97–105.

Zhu, F., Liu, J., Lai, X., Xiao, Y., Prakapenka, V., Bi, W., Alp, E.E., Dera, P., Chen, B., and Li, J. (2020) Synthesis, Elasticity, and Spin State of an Intermediate $MgSiO_3$-$FeAlO_3$ Bridgmanite: Implications for Iron in Earth's Lower Mantle. Journal of Geophysical Research: Solid Earth, 125, e2020JB019964.

Zhu, S., Liu, J., Hu, Q., Mao, W.L., Meng, Y., Zhang, D., Mao, H., and Zhu, Q. (2019) Structure-Controlled Oxygen Concentration in Fe2O3 and FeO2. Inorganic Chemistry, 58, 5476–5482.